Magnetism of the Acapulco Primitive Achondrite and Implications for the Evolution of Partially Differentiated Bodies

Elias N. Mansbach[1], Benjamin P. Weiss[1], Neesha R. Schnepf[2], Eduardo A. Lima[1], Cauê S. Borlina[1,3], Nilanjan Chatterjee[1], Jérôme Gattacceca[4], Minoru Uehara[4], Huapei Wang[5]

[1]Department of Earth, Atmosphere, and Planetary Sciences, Massachusetts Institute of Technology, Cambridge, MA, USA
[2]Laboratory for Atmospheric and Space Physics, University of Colorado, Boulder, CO, USA
[3]Department of Earth and Planetary Science, Johns Hopkins University, Baltimore, MD, USA
[4]CNRS, Aix Marseille Université, IRD, INRAE, CEREGE, Aix-en-Provence, France
[5]School of Geophysics and Geomatics, China University of Geosciences, Wuhan, China

Corresponding author: Elias Mansbach (mansbach@mit.edu)

Key Points:

- We studied the rock magnetics properties of the primitive achondrite Acapulco to pave the way for future paleomagnetic investigations
- While bulk samples are poor recorders, silicate grains with metal inclusions may retain stable magnetizations over 4.5 billion years
- The presence of the mineral tetrataenite indicates that Acapulco experienced slow cooling (~5×10^3 °C Ma^{-1}) at temperatures ~320°C

Abstract

Primitive achondrites like the acapulcoites-lodranites (AL) clan are meteorites that formed on bodies in the process of forming a metallic core, providing a unique window into how early solar system processes transformed unmelted material into differentiated bodies. However, the size and structure of the parent body of ALs and other primitive achondrites are largely unknown. Paleomagnetism can establish the presence or absence of a metallic core by looking for evidence of a dynamo magnetic field. We conducted a magnetic study of the Acapulco acapulcoite to determine its ferromagnetic minerals and their recording properties. This is the first detailed rock magnetic and first paleomagnetic study of a primitive achondrite group. We determined that metal inclusions located inside silicate grains consist of two magnetic minerals, kamacite and tetrataenite, which have robust recording properties. However, the mechanisms and timing by which these minerals acquired any natural remanent magnetization are unknown. Despite this, Acapulco has not been substantially remagnetized since arriving on Earth and therefore should retain a record dating to 4.55 billion years ago. Future studies could characterize this record by using high resolution magnetometry measurements of individual grains and developing an understanding of how and when they became magnetized. Our discovery of tetrataenite in ALs provides the first mineralogical evidence for slow cooling (~5×10^3 °C Ma^{-1}) of the AL parent body at low temperatures (~320°C). Its presence means that the AL parent body is unlikely to have been catastrophically disrupted at AL peak temperatures (~1200°C) without subsequent reaccretion.

Plain Language Summary

Primitive achondrites are a rare group of meteorites that formed as the result of partial melting on their parent bodies, and therefore provide key insights into metal-silicate differentiation in the early solar system. However, the sizes and structures of their parent bodies remain uncertain. Here, we conduct a rock magnetic study of the Acapulco acapulcoite to identify the ferromagnetic recorders and to determine if the meteorite could retain a ~4.55 billion year old magnetic record. We find sub-micrometer sized kamacite and tetrataenite grains embedded in silicate grains that should retain a stable magnetization. The presence of tetrataenite suggests slow cooling of acapulcoites at low temperatures, indicating that the parent body could not have been catastrophically disrupted without later reaccretion.

1 Introduction

Meteorites are divided into three classifications. Chondrites are unmelted accretional aggregates of nebular materials, achondrites are melts associated with igneous differentiation on their parent bodies, and primitive achondrites are melt residues from parent bodies that underwent incomplete differentiation (Weisberg et al., 2006). Collectively, they provide records of the thermochemical and geophysical evolution of planetesimals, the <~500 km radius rocky-icy parent bodies that served as the building blocks for modern planets (Weiss & Elkins-Tanton, 2013). It is typically assumed that many (or perhaps even all) achondrites formed from melting of materials that once formed chondrites. As such, primitive achondrites are of interest because they represent intermediate stages of differentiation in this process and therefore contain unique records of the timescales and mechanisms by which planetary melting processes transformed nebular material into compositionally segregated structures.

The acapulcoites-lodranites (ALs) are a clan of primitive achondrites composed of two meteorite groups, the acapulcoites and the lodranites. Acapulcoites have bulk near-chondritic compositions that are depleted in Fe-Ni-S melt (< 5 vol.% partial melting), average grain diameters of 150-230 μm, and equigranular textures with abundant triple junctions (Keil & McCoy, 2018; McCoy et al., 1996). Acapulcoite mineralogy consists mostly of olivine, pyroxenes, plagioclase, and Fe-Ni-S compounds (Keil & McCoy, 2018; Palme et al., 1981). Some acapulcoites possess mm- to cm-scale metal veins likely representing the initial stages of melt migration on the parent body (Keil & McCoy, 2018; McCoy et al., 1997). They are estimated to have reached peak temperatures of 980 – 1170°C during prograde metamorphism (Keil & McCoy, 2018; McCoy et al., 1996). Lodranites are coarser grained than acapulcoites (average grain diameter 540-700 μm), also depleted in Fe-Ni-S melt, and are sometimes additionally depleted in plagioclase-pyroxene (5 - 20 vol.% partial melting), indicating that they were heated to higher temperatures (1150-1200°C) (Bild & Wasson, 1976; Keil & McCoy, 2018; McCoy et al., 1996). The combination in ALs of a near-chondritic composition largely undepleted in incompatible elements and textural evidence for subsolidus recrystallization with limited melting is the hallmark of a primitive achondrite group. ALs are thought to represent a single, distinct parent body from known meteorites based on unique oxygen isotope compositions and abundances of volatiles, lithophile, and siderophile elements (Greenwood et al., 2017; Greenwood et al., 2012; Keil & McCoy, 2018).

The metal in the eponymous acapulcoite Acapulco, which comprises 11.3 – 22.7 wt.% of the meteorite (Palme et al., 1981; Zipfel et al., 1995), is reported to occur in two forms: (1) intergrown 50 – 500 μm-sized assemblages of kamacite (α-$Fe_{1-x}Ni_x$ for $x < 0.06$) and zoned

taenite (γ-$Fe_{1-x}Ni_x$ for $0.06 \lesssim x \lesssim 0.5$) located interstitially between silicate grains; and (2) sub-μm to μm-sized kamacite and taenite inclusions in the cores of olivine and pyroxene grains (inclusion average $x = 0.08$), henceforth called metal-bearing silicates (MBSs) (Fig. 1) (El Goresy et al., 2005; Keil & McCoy, 2018; Palme et al., 1981; Zipfel et al., 1995). The carriers of any remanent magnetization have not been identified in Acapulco but could possibly be kamacite in interstitial metal assemblages (form 1), inclusions in MBSs (form 2) and/or tetrataenite (γ"-$Fe_{0.5}Ni_{0.5}$) in the high-Ni rims of zoned taenite (form 1) interstitial grains and MBSs (form 2). These MBSs are of great interest for possible paleomagnetic studies because they resemble dusty olivine chondrules (DOCs) that have been found to be high-fidelity magnetic recorders in LL and CO chondrites (Borlina et al., 2021; Fu et al., 2014).

Despite the extensive petrological, geochemical, and geochronological analyses of ALs, the size, structure, and thermal history of their parent body remain poorly constrained. Previous thermal modeling suggests that ALs formed in the upper 25 km of a body with a radius of 35 – 270 km, with the possibility of an Fe-Ni-S core (Golabek et al., 2014; Neumann et al., 2018; Touboul et al., 2009). Additionally, differences in cooling rates determined by geochronometers and mineral indicators have led to suggestions the parent body was disrupted while ALs were above ~500°C and then potentially reaccreted (Göpel & Manhès, 2010; Lucas et al., 2022), although an alternate explanation might be the unroofing of overlying material as suggested for IVA irons (Yang et al., 2007). Paleomagnetism can be used to search for evidence of a dynamo magnetic field, which would be direct evidence that the body possessed an advecting, liquid metal core with a diameter of at least several tens of km (Bryson et al., 2019; Weiss et al., 2010). It would further suggest that at the time of magnetization acquisition, at least the central portion of the parent body efficiently segregated metal and silicates.

The goal of this study is to address the following questions for Acapulco: 1) Does Acapulco retain a pre-terrestrial natural remanent magnetization (NRM)? That is, has the meteorite been substantially magnetized since falling to Earth or might it retain an NRM pre-dating its arrival? 2) Is Acapulco capable of retaining an interpretable early solar system magnetic record to the present day? and 3) How can the paleomagnetism and rock magnetic properties of Acapulco constrain the parent body's interior structure and thermal evolution? To answer these questions, it is vital to inventory the ferromagnetic mineralogy of the meteorite and constrain its recording properties, its form of NRM [e.g., thermoremanent magnetization (TRM), crystallization remanent magnetization (CRM), and/or shock remanent magnetization (SRM)], and at what temperature that NRM could have been acquired. Here, we determine the answer to the above questions for both the large interstitial metal grains in bulk samples and the metal inclusions in MBSs. While there has been an initial study of the rock magnetic properties of primitive achondrites (Rochette et al., 2009) and a paleomagnetic study of IAB iron meteorites (Nichols et al., 2018), which have been proposed to originate from the same parent body as the winonaite primitive achondrite group, no paleomagnetic study has previously been conducted on a primitive achondrite meteorite.

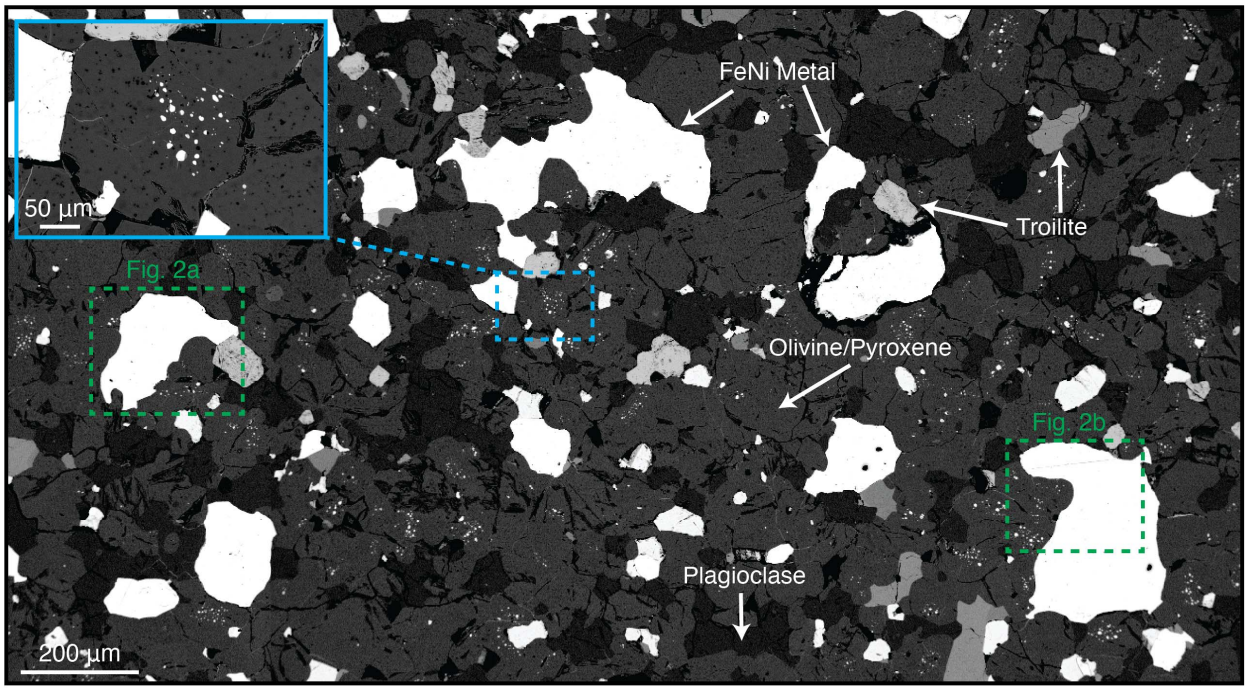

Figure 1. Backscattered electron (BSE) image of Acapulco thin section USNM 5967-1 showing FeNi metal, troilite (FeS), plagioclase, and olivine and pyroxene. The multidomain, interstitial metal grains (50 µm to 1 mm in size) dominate the NRM of the bulk samples, making them nonideal magnetic recorders. Blue outlined inset shows a metal-bearing silicate (MBS). Visible are <10 µm FeNi metal grains that may extend into the single domain (SD) or pseudo-single domain (PSD) size range and therefore may have optimal magnetic recording properties. Grains that appear in other figures are outlined and labeled.

2 Materials and Methods

2.1 The Acapulco Meteorite

We selected Acapulco for analysis because previous studies indicated it may have rock magnetic properties favorable for paleomagnetism. In particular, it is one of only two known AL falls and therefore unlikely to have been weathered on Earth [Acapulco has little to no reported weathering products (Dhaliwal et al., 2017)] or exposed to a hand magnet from a collector (Vervelidou et al., 2023; Weiss et al., 2010). Additionally, Acapulco retains a fusion crust, which can be used to determine whether the interior of the sample has been remagnetized through a fusion crust baked contact test (see below) (Weiss et al., 2010). Acapulco is essentially unshocked [stage S1, with peak pressures < 5 GPa (Palme et al., 1981)] meaning it should have not have acquired a significant SRM or been significantly shock demagnetized. Furthermore, $^{40}Ar/^{39}Ar$ dating of plagioclase in Acapulco yields ancient ages of 4554 ± 43 Ma (Renne, 2000). For cooling rates between 100 and 100,000°C Ma^{-1}, the Ar closure temperature for ~100-200 µm-sized plagioclase is 300-400°C, which is well below the Curie temperature of kamacite (780°C) and spans the ordering temperature of tetrataenite (320°C). Thus, the $^{40}Ar/^{39}Ar$ age

places a lower bound on the date of any NRM acquisition by kamacite and an upper bound for tetrataenite. The ancient $^{40}Ar/^{39}Ar$ age also suggests that the samples have not experienced significant metamorphism or impact heating since initial cooling (Palme et al., 1981).

For this study, a 4.02 g piece of Acapulco (USNM 5967) with a fusion crust was provided by the Smithsonian National Museum of Natural History. This sample has a fusion crust on one side that extends < 0.5 mm into the interior. From this main mass, we extracted nine mutually oriented bulk subsamples (masses 5-50 mg), labeled NMMAC1-8 and NMMAC12, containing MBSs and interstitial metal grains. These were cut from the main mass in a transect perpendicular to the fusion crust to sample both the crust and the interior of the sample (Fig. S1). Three subsamples (NMMAC 1, 5, 12) contained fusion crust and the other six (NMMAC 2-4, 6-8) sampled the interior at various distances up to a maximum of 7.5 mm from the fusion crust. All samples were photographed and mutually orientated to within 5º uncertainty. In addition to the bulk subsamples, seven MBSs labeled MBS 2-5, 8-10 (masses ~ 0.12 ± 0.06 mg) were extracted from a thick section called NMMAC11 (Figs. S2, S3). The MBSs were also photographed and mutually oriented relative to each other and the bulk samples within 5º. We acquired the transect of bulk subsamples from the fusion crust into the interior to determine if the meteorite has been remagnetized after falling to Earth. In particular, because the fusion crust is expected to have acquired a TRM from atmospheric heating, if the meteorite has been remagnetized since landing on Earth (e.g., via a hand magnet, weathering and/or viscous remagnetization in Earth's field), the magnetization directions of the fusion crust and the interior subsamples would be clustered.

In addition to a bulk sample, a 30-µm thin section of Acapulco (USNM 5976-1) was provided by the Smithsonian Museum of Natural History. The thin section was used primarily to determine the size, texture, habit and composition of the metal grains in Acapulco.

2.2 Compositional Methods

We collected backscattered electron (BSE) microscopy images and quantitative compositional measurements of polished MBSs and interstitial metal grains using wavelength dispersive spectroscopy (WDS) on a JEOL JXA-8200 Superprobe electron microprobe machine at the Department of Earth, Atmospheric, and Planetary Sciences at MIT. Following WDS measurements but prior to BSE imaging, the samples were etched with 2% nital for 20 seconds to enhance grain boundaries associated with metallographic exsolution textures. Additional secondary electron (SE) images and quantitative compositional measurements using electron dispersive spectroscopy (EDS) were acquired using a Merlin Zeiss Field Emission Gun-SEM in the MIT Material Resources Laboratory. All BSE images and EDS and WDS measurements were conducted on thin section USNM 5967-1.

2.3 Magnetic Methods

We conducted nearly all magnetic measurements in the Massachusetts Institute of Technology (MIT) Paleomagnetism Laboratory. A Enterprises Superconducting Rock

Magnetometer (2G SRM) 755 [2σ noise floor of 0.99×10^{-12} Am^2; Fig. S5 in Wang et al. (2017)] equipped with an automatic sample handing and coil system was used for alternating field (AF) demagnetization of bulk and MBS sample NRMs. Bulk samples were demagnetized to up to a maximum of 85 or 145 mT in steps of 0.5 – 1 mT and their magnetizations were measured using the SRM. MBS samples were AF demagnetized to up a maximum field ranging between 500 – 900 mT in steps of 10 – 100 mT. Due to the weak NRMs of the MBSs (~ 10^{-11} – 10^{-12} Am^2), we extracted them from the meteorite (see Supplement Section 1) and their magnetizations were measured using a superconducting quantum interference device (SQUID) microscope (noise floor of 6×10^{-15} Am^2), which maps the out-of-the-page (z) component of the magnetic field produced by the sample ~200 μm above the MBS (Weiss et al., 2007). The net magnetic moments of MBS samples were determined by performing a dipole fit to the SQUID microscope maps (Lima & Weiss, 2016). For MBSs measured in the SQUID microscope, three maps were made at each AF step <145 mT to reduce spurious anhysteretic remanent magnetization (ARM) (Tikoo et al., 2012). Between 145 and 420 mT, maps were made after AF demagnetization along each of the three orthogonal axes; these were used to correct for any gyroremanent magnetization acquired during AF demagnetization by averaging the moments measured after each AF application following the Zijderveld-Dunlop method (Stephenson, 1993). Demagnetization above 420 mT was achieved using IRMs applied in alternating directions and decreasing in strength (i.e., DC demagnetization). Magnetic optical imaging (MOI) was performed at CEREGE in France. Directions of NRM components and their maximum angle of deviation (MAD) values, which provide a measure of angular uncertainty in the components (Khokhlov & Hulot, 2015), were determined by principal component analysis (PCA) (Kirschvink, 1980).

After NRM AF demagnetization, ARMs were applied to bulk samples (130 mT AC field, 200 μT bias field) and MBSs (145 mT AC field, 200 μT bias field) to simulate acquisition of a TRM acquired during cooling (Dunlop & Argyle, 1997). AF demagnetizations of these ARMs were compared to that of NRM to determine if the NRM is consistent with a TRM.

The magnetic recording properties of bulk samples and MBSs were assessed through applications and subsequent AF demagnetizations of isothermal remanent magnetizations (IRMs) on previously demagnetized samples. We used AF demagnetization of a 1 T IRM both to estimate coercivity spectra, which we used to help identify ferromagnetic minerals, and to constrain the origin of NRM overprints through paleointensity estimations. The paleointensity (B_{int}) was calculated as:

$$\boldsymbol{B_{int} = \frac{\Delta NRM}{\Delta IRM} \cdot a}$$

where $\boldsymbol{\Delta NRM}$ and $\boldsymbol{\Delta IRM}$ is the change in NRM and IRM respectively during AF demagnetization and a = 3000 μT is an experimentally-determined correction factor to account for the ratio of IRM to TRM for kamacite (Bryson et al., 2017; Tikoo et al., 2014).

Thermal demagnetization of an IRM was conducted to aid in ferromagnetic mineral identification in MBSs through determination of Curie points. A 1 T IRM was applied to MBSs 5, 8, and 10 and heating was performed using a Magnetic Measurements oven in a controlled atmosphere to limit alteration or creation of new magnetic minerals during heating (Suavet et al., 2014). Consistent with estimates of the oxygen fugacity for Acapulco formation based on

olivine-chromite thermometry (Benedix & Lauretta, 2006), we set the oxygen fugacity to -2.3 log units below that of the iron-wüstite (IW) buffer. Heating was conducted in steps of 10 – 50ºC up to 770 ºC with the full heating and cooling time taking 20 minutes total for each step.

The location and distribution of the magnetic remanence carriers in MBSs were determined using a quantum diamond microscope, which maps the magnetic field with a ~5 μm spatial resolution at a distance of ~10 μm above the sample [moment sensitivity 1×10^{-14} Am^2 (Fu et al., 2020; Glenn et al., 2017)].

3 Results

To address the three questions in Section 1, we conducted electron, optical, transmission X-ray and magnetic microscopy and compositional analyses of the metal in Acapulco, analyzed the magnetic properties of the metal, and studied the NRM of bulk samples and individual MBSs. These three investigations allow us to determine the ferromagnetic mineralogy, the recording properties of the minerals, and whether Acapulco has been magnetized since falling to Earth.

3.1 Microscopy and Compositional Analysis of Acapulco Metal

We found that interstitial metal grains range in size from 50 μm to 1 mm (Fig. 1). Our BSE images and wavelength dispersive spectroscopy (WDS) transects of Acapulco 30-μm thin section USNM 5967-1 show that the interstitial metal grains consist of two phases: (A) kamacite (5-6 wt.% Ni) and (B) zoned taenite exhibiting Ni gradients from 13 wt.% near the center of the grains to 37 wt.% near the rim (Fig. 2a, b). The zoning is consistent with the "M" shaped profile seen in iron meteorites that forms during subsolidus cooling due to the slower diffusion of Ni through taenite compared to kamacite (Yang & Goldstein, 2005). We did not observe any cloudy zone microstructures in BSE images of the thin section after nital etching or in magneto-optical images (Fig. S5, S6).

BSE images of the center of zoned taenite interstitial metal grains show the presence of plessite, a metallic micro- and/or nanostructure that forms from the subsolidus decomposition of martensite (α_2-FeNi) into high- and low- Ni phases [Fig. 2c, (Goldstein & Michael, 2006)]. EDS spot measurements of the μm-sized high-Ni precipitates show that their Ni contents reach up to ~50 wt.% and therefore should be in the form of either taenite or tetrataenite.

Transmission X-ray microscopy shows that unlike the >50 μm interstitial metal grains, MBSs possess inclusions with sizes <0.4 – 13 μm (Fig. S4). BSE images show that MBS metal grains consist of two types: (I) a low-Ni FeNi metal phase with some grains possessing a <1 μm, high-Ni rim (Fig. 3a, b), and (II) an intergrowth of high-Ni precipitates in a low-Ni matrix (Fig. 3b, c). Our WDS measurements of type I grains (Fig. 3b) show that the low-Ni phase is kamacite (<6 wt.% Ni) and that the high-Ni rim, which can reach up to ~50 wt.%, is either taenite or tetrataenite. No Ni compositional gradient is observed in these grains.

Type II metal grains exhibit a plessitic microstructure similar to that observed in the interstitial metal grains, although on a smaller scale (generally sub-µm precipitates compared to the µm-sized precipitates in the interstitial metal). Although the small sizes of the precipitates prohibit determination of their composition by EDS and WDS, it is likely that as for plessite in the interstitial grains, some metal grains in the MBS plessite have compositions reaching ~50 wt.% Ni given that such a Ni-rich composition is a natural outcome of plessite formation during slow cooling (Goldstein & Michael, 2006).

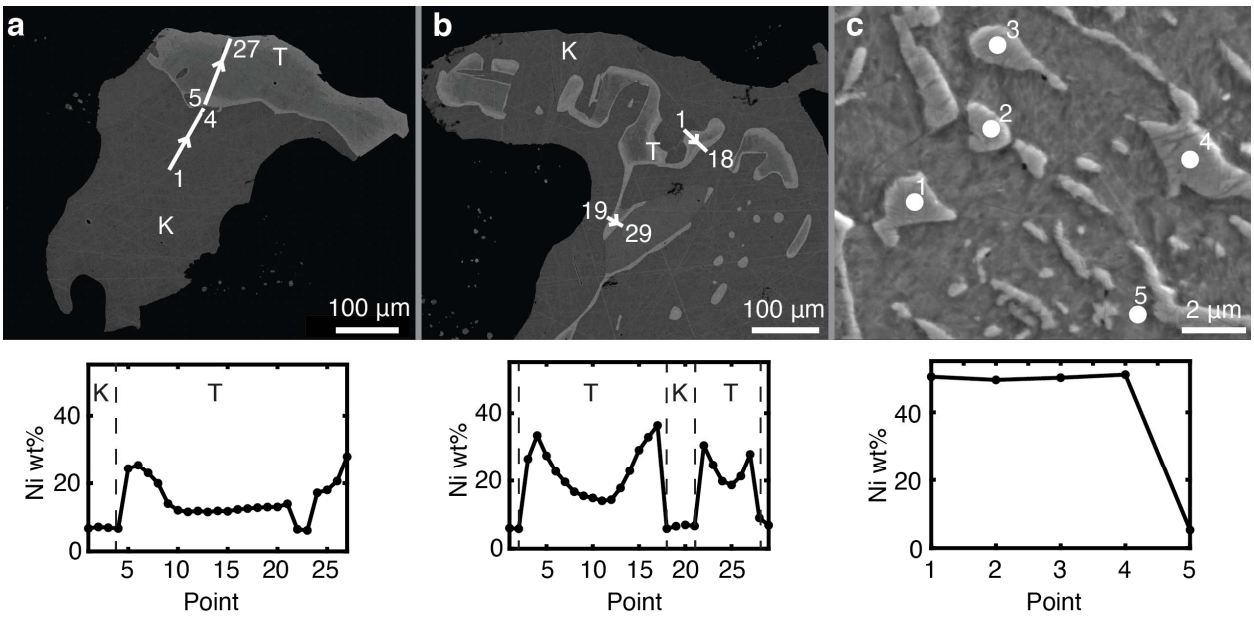

Figure 2. Electron microscopy images and compositions of interstitial metal. **a)** BSE image (top) and corresponding WDS measurements (bottom) of an interstitial metal grain. White line with arrows in the BSE image shows location and direction of the WDS transect. Brightness denotes atomic number, with Fe darker than Ni. These data show that the metal grain is a composite of at least two phases. The bottom section of the grain is uniform in texture and composition with a mean Ni content of 6 wt. %, indicating it is kamacite. The top portion exhibits higher Ni and a zoned composition reaching up to ~30 wt.% Ni in the rim and down to ~13 wt.% Ni in the center. **b)** BSE image of another metal grain (top) and corresponding WDS transects cover two Ni gradients in a zoned taenite. The maximum and minimum Ni compositions are 37 and 7 wt.%, respectively. **c)** Secondary electron image of plessite in the center of a zoned taenite in an interstitial metal grain (not shown). The precipitates are composed of ~50 wt.% Ni, and therefore taenite or tetrataenite, while the matrix is ~5 wt.% Ni and therefore kamacite. K = kamacite, T = taenite.

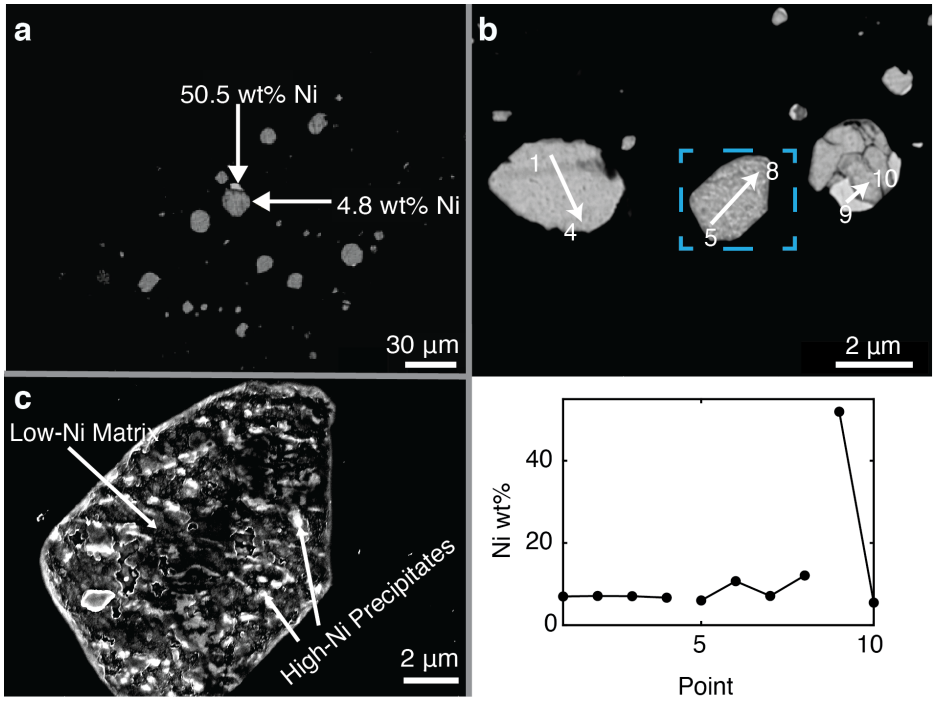

Figure 3. Microscopy images and compositions of MBS metals in USNM 5971-1. **a)** BSE image of metal inclusions in an MBS. Most inclusions have apparently homogenous Ni abundances in the range of kamacite with occasional inclusions (<1% of total area) possessing brighter, high-Ni rims [type I grains]. These grains have not been etched with nital. **b)** Top: BSE image of metal inclusions in a separate MBS from a) showing two type I grains on the far left and right and a type II grain in the center. The grains have been etched with nital. Bottom: WDS compositions at the locations marked in the BSE image. **c)** Detailed BSE image of the boxed metal inclusion in b) showing a plessitic microstructure.

3.2 NRM Demagnetization

W analyzed the NRMs of nine mutually oriented bulk subsamples (5-50 mg) of fusion-crusted specimen USNM 5967 (labelled NMMAC1-8,12; Fig. S1) in a transect from the exterior to the interior. Our AF demagnetization revealed that three fusion-crusted samples each possessed a common low coercivity (LC) component, denoted LCf, that unblocked between 0 and 3 – 14 mT depending on the sample (Fig. 4a, c; Fig. S12). Similarly, all interior bulk samples had a common LC component, denoted LCi, that unblocked between 0 and 5 – 15 mT (Figs. 4b, d; Fig. S12). While all bulk samples had a LCi or LCf component, the high average MAD values of 16.8° for these components indicate large directional scatter during demagnetization over the component AF ranges. None of the LCf or LCi components for the fusion-crusted or interior samples have a deviation angle (DANG) less than their MAD value (Tauxe & Staudigel, 2004), suggesting they are not origin-trending and therefore not primary components (Table S3).

The average directions of the LCi and LCf components are 58.8° apart and do not fall within each other's 95% confidence circles (Fig. 4e). Because the LCi and LCf α_{95} ellipses overlap, we conducted a common mean bootstrap test (Tauxe, 2010) to determine if the groups of LCi and LCf components share average directions. The two distributions failed the test, indicating that their mean directions are statistically distinct to 95% confidence. Out of the nine samples, we estimated paleointensities for six samples. The paleointensities of the LCf components for the fusion-crusted samples NMMAC1 and NMMAC12 are 82.1 ± 15.7 μT (uncertainties here and elsewhere are 95% confidence intervals) and 79.9 ± 20.3 μT, respectively. The average paleointensity of the four LCi components calculated for interior samples NMMAC2, NMMAC3, NMMAC7, and NMMAC8 is 42.2 ± 23.1 μT (Table S3).

We found that seven of the nine bulk samples possessed a trending medium coercivity component (denoted MCi for interior samples and MCf for fusion-crusted samples) that unblocked starting from the end to the LCi/LCf component to 10 – 66 mT depending on the sample. After removal of the MCf and MCi components, there were no further identifiable trending components in any sample. We note that no effects were seen from gyroremanent magnetization at large demagnetization fields for any sample [e.g., (Garrick-Bethell et al., 2009)].

Unlike the LCi and LCf components, the individual MCi and MCf component directions are not well-clustered (Fig. 4e). Two of the fusion-crusted samples (NMMAC5 and 12) show similar (9° difference) MCf component directions, but the direction of the third fusion-crusted MCf differs by 106°. The average MAD of the MCi and MCf components is 31.9°, highlighting the scatter in the demagnetization of the samples despite noticeable magnetization trends. The MCf components of bulk samples NMMAC1, 5, and 12, and the MCi component of bulk sample NMMAC6 have DANG < MAD, suggesting they may be origin-trending (Table S3). However, the MAD values of these samples are >30°, and therefore the components are unlikely to be a primary magnetic record.

AF demagnetization of the NRMs of five MBSs did not reveal any clear components, although MBS3 and MBS9 may possess a weak LC component (Figs. 5a-c; S13). The NRM of each sample did not exhibit consistent decreases in intensity. Instead, they were clustered (Fig. 5b) and/or inconsistently jumped in direction with each AF step (Fig. 5c). Similar to the bulk samples, no effects were seen from gyroremanent magnetization. The NRM directions of the MBSs prior to AF demagnetization (Fig. 5d) are scattered and not consistent with the LCi or LCf directions.

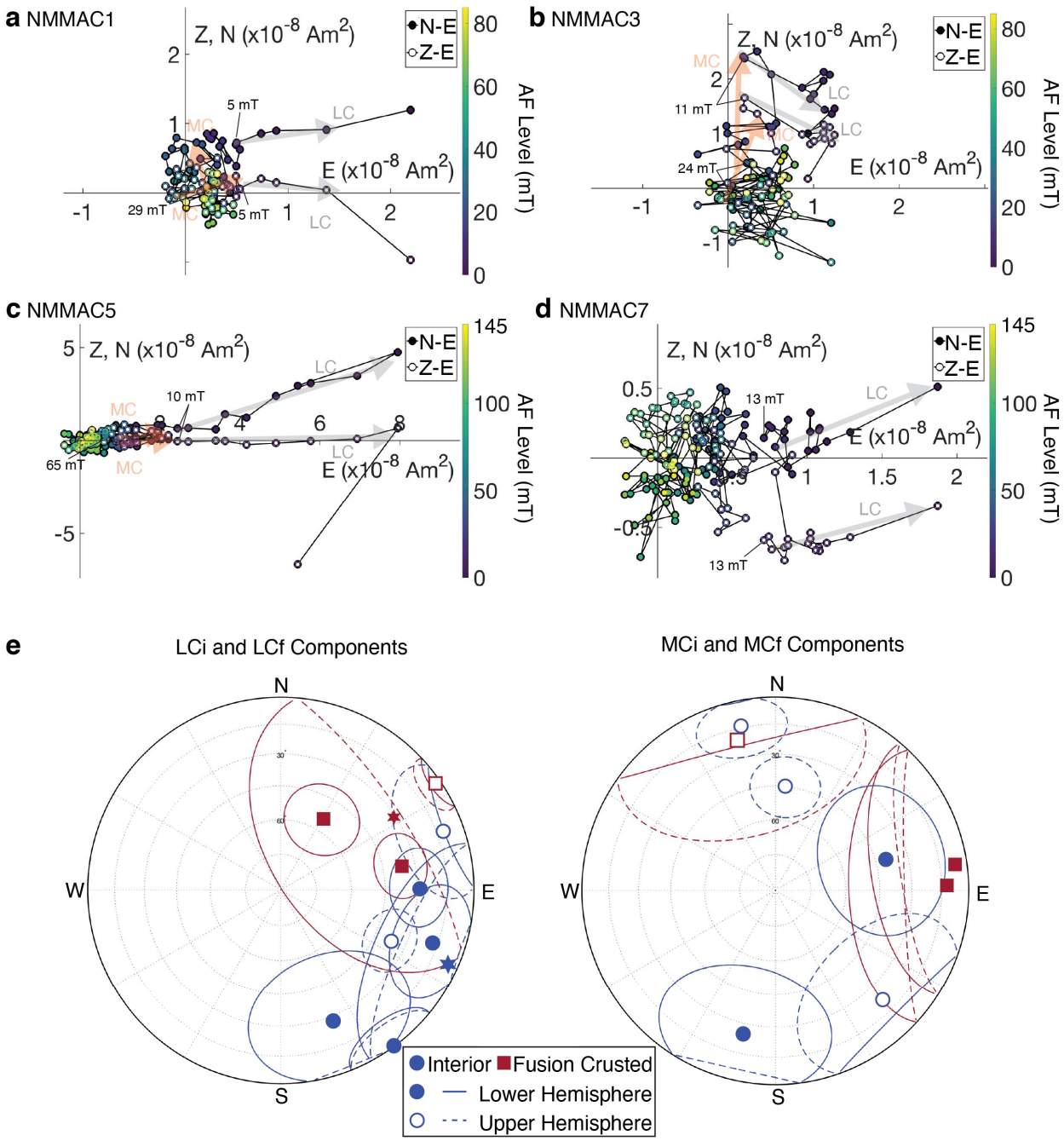
a NMMAC1
Z, N (x10^-8 Am^2)
E (x10^-8 Am^2)
N-E
Z-E
AF Level (mT)
5 mT
29 mT
MC
LC
b NMMAC3
11 mT
24 mT
c NMMAC5
10 mT
65 mT
d NMMAC7
13 mT
e
LCi and LCf Components
MCi and MCf Components
N
S
E
W
Interior
Fusion Crusted
Lower Hemisphere
Upper Hemisphere

353 **Figure 4.** AF demagnetization of bulk sample NRMs measured with the SRM. **(a-d)**
354 Orthographic projections of endpoints of NRM vectors on the north-east (N-E) and up-east (Z-E)
355 planes. LCi/LCf components are denoted by the grey arrows and MCi/MCf components are
356 denoted by the orange arrows. (a) Fusion-crusted sample NMMAC1: an LCf component
357 unblocked between 0 and 4.5 mT and an MC component unblocked between 5.5 and 29 mT. (b)
358 Interior sample NMMAC3: an LCi component unblocked between 0 and 10 mT and an MC
359 component unblocked between 11 and 24.5 mT. (c) Fusion-crusted sample NMMAC5: An LCf
360 component unblocked between 0 and 14 mT and an MC component unblocked between 14.5 and
361 66 mT. (d) Interior sample NMMAC7: an LCi component unblocked between 0 and 13 mT.
362 Color bars to the right of each panel in (A-D) denote AF level for each step. **e)** Equal area
363 stereographic projection showing LCi/LCf (left) and MCi/MCf (right) component directions for
364 the bulk samples. Fusion-crusted samples are denoted as red squares and interior samples as blue
365 circles. The average fusion-crusted LC direction (red star) and average interior sample LC
366 direction (blue star) fall outside each other's 95% confidence circles, but their confidence circles
367 overlap.

368

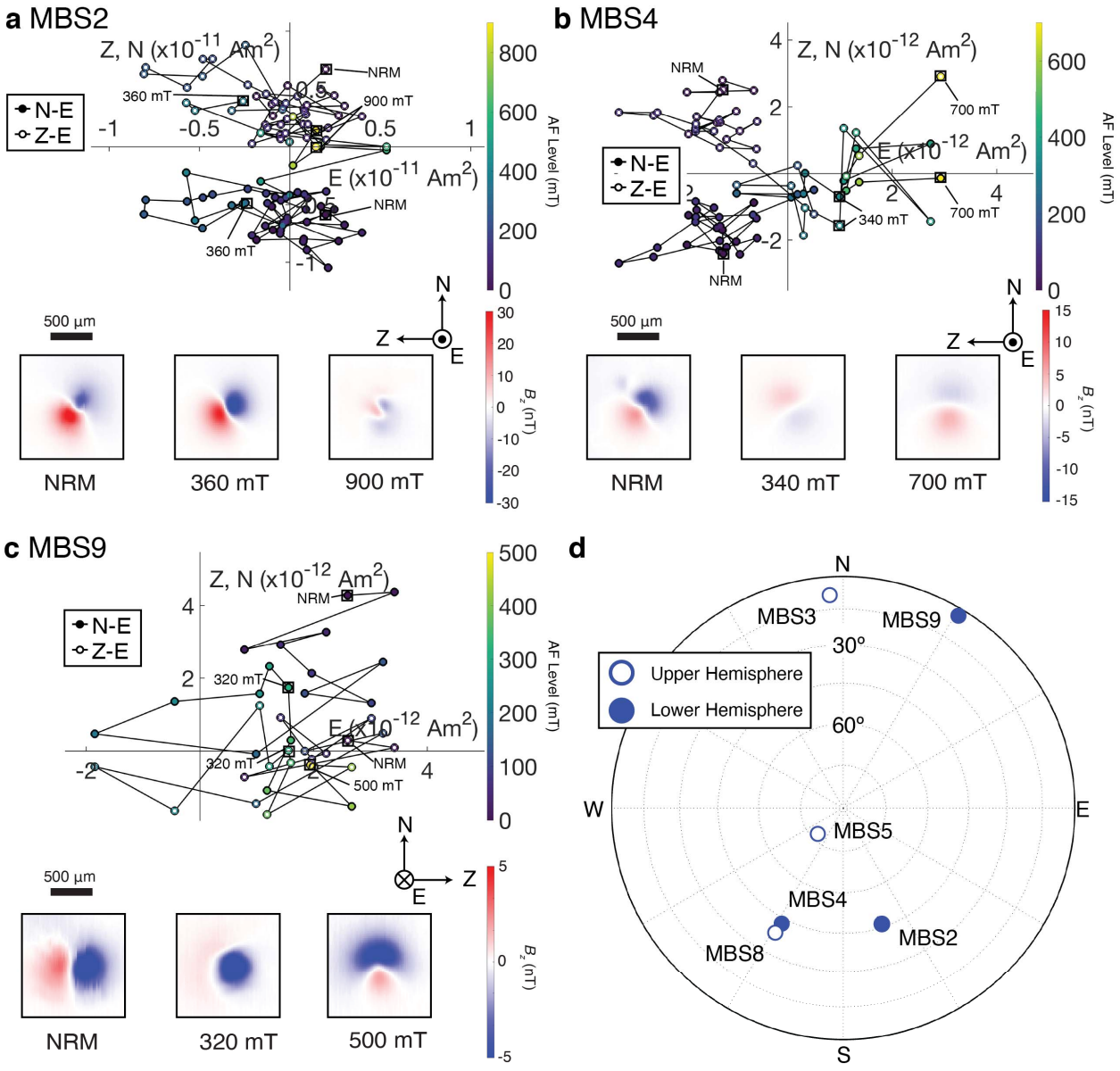

Figure 5. NRM demagnetization of MBSs as measured in the SQUID microscope. **(a-c)** Orthographic projections of endpoints of NRM vectors on the northeast (N-E) and up-east (Z-E) planes: MBS2 (a) MBS4 (b) and MBS9 (c). Representative SQUID microscope maps at selected field steps for each MBS are shown below and are associated with boxed steps on the orthographic projections. **d)** Equal area stereonet showing the NRM direction of MBSs. Open (closed) circles represent NRM directions in the upper (lower) hemisphere of the stereonet.

379 3.3 Magnetic Properties

380 AF demagnetization of a saturating 1 T IRM applied to two fusion-crusted samples,
381 NMMAC1 and NMMAC12, and two interior samples, NMMAC6 and NMMAC7, revealed
382 different behaviors (Fig. 6a). The fusion-crusted samples show a rapid drop in magnetization at
383 lower AF levels, dropping to 50% of their IRM moment, known as the median destructive field
384 (MDF), at 9 mT and 14.5 mT for NMMAC12 and NMMAC1 respectively. Comparatively, the
385 interior samples show a slower rate of decrease in moment with AF level and MDFs of 30 mT
386 and 47 mT for NMMAC7 and NMMAC6, respectively.

387 By the 130 mT AF step, the two interior samples still retained 19-25% of their IRM while
388 the fusion-crusted samples had less than 1% of their IRM, indicating that the interior samples
389 contain a larger fraction of recorders with microcoercivities >130 mT (Fig. 6a). This behavior is
390 also seen in the coercivity spectra of the samples (Fig. 6b), calculated as the derivative of the
391 curve in Figure 6A with respect to AF level: the fusion-crusted samples have a factor of 2 larger
392 rate of magnetization loss per AF level compared to the interior samples. However, both interior
393 and fusion-crusted samples only show a peak in the coercivity spectrum at low AF levels,
394 suggesting that their magnetization is carried primarily by lower-coercivity grains.

395 The AF demagnetization behavior of ARMs also differed for fusion-crusted samples (Fig.
396 6c) compared to interior samples (Fig. 6d). Fusion-crusted samples show a monotonic decrease
397 in moment until ~50 mT, after which the moment fluctuates around a constant value. By
398 comparison, the ARMs for the interior samples (Fig. 6d) experienced monotonic decreases in
399 moment until AF levels of 10-30 mT depending on the sample, after which their moments
400 showed no further demagnetization with increasing AF level.

401 Quantum diamond microscopy (Glenn et al., 2017) confirms that the main magnetization
402 carriers of the MBSs are metal inclusions in the grain interiors (Fig. S9). AF demagnetization of
403 a 1 T IRM for MBSs 4, 5, and 8 shows that the silicates retain >22-41% of their initial
404 magnetization after being demagnetized to 120 mT (Fig. 7a). The average MDF of the three
405 MBSs is 65.1 mT, 5.5 and 1.7 times higher than the average MDFs for the fusion-crusted bulk
406 samples and interior bulk samples, respectively. Previous AF demagnetizations of 1 T IRMs in
407 DOCs indicate they retain only 8-24 % of their IRM after being demagnetized to 120 mT (Fig.
408 7a). Thus, there is a population of grains in MBSs with microcoercivities exceeding the
409 maximum coercivities observed for DOCs, which are amongst the highest fidelity known
410 magnetic recorders for chondrites (Borlina et al., 2021; Fu et al., 2014; Lappe et al., 2011; Lappe
411 et al., 2013). However, the higher rate of loss of magnetization between 0 - 90 mT for MBSs
412 compared to DOCs suggests that MBSs have a larger fraction of metal grains with coercivities
413 below 90 mT, which are very likely the >1 μm metal inclusions visible in reflected light images
414 (Fig. 1).

415 Controlled atmosphere thermal demagnetizations of a 1 T IRM applied to three MBSs
416 showed a progressive loss of magnetization in all MBSs during heating from room temperature
417 to 500ºC (Fig. 7b). The IRM then exhibited a sharp 37 - 64% drop between 500 and 540ºC,
418 consistent with the Curie temperature of taenite with 49-52 wt.% Ni (Swartzendruber et al.,
419 1991), which was present prior to demagnetization and/or formed from the disordering of
420 tetrataenite by laboratory heating (Dos Santos et al., 2015). We also observed the loss of a 300-

500 mT high coercivity phase after heating to 600ºC in first-order reversal curve (FORC) diagrams made on bulk samples (Fig. S8).

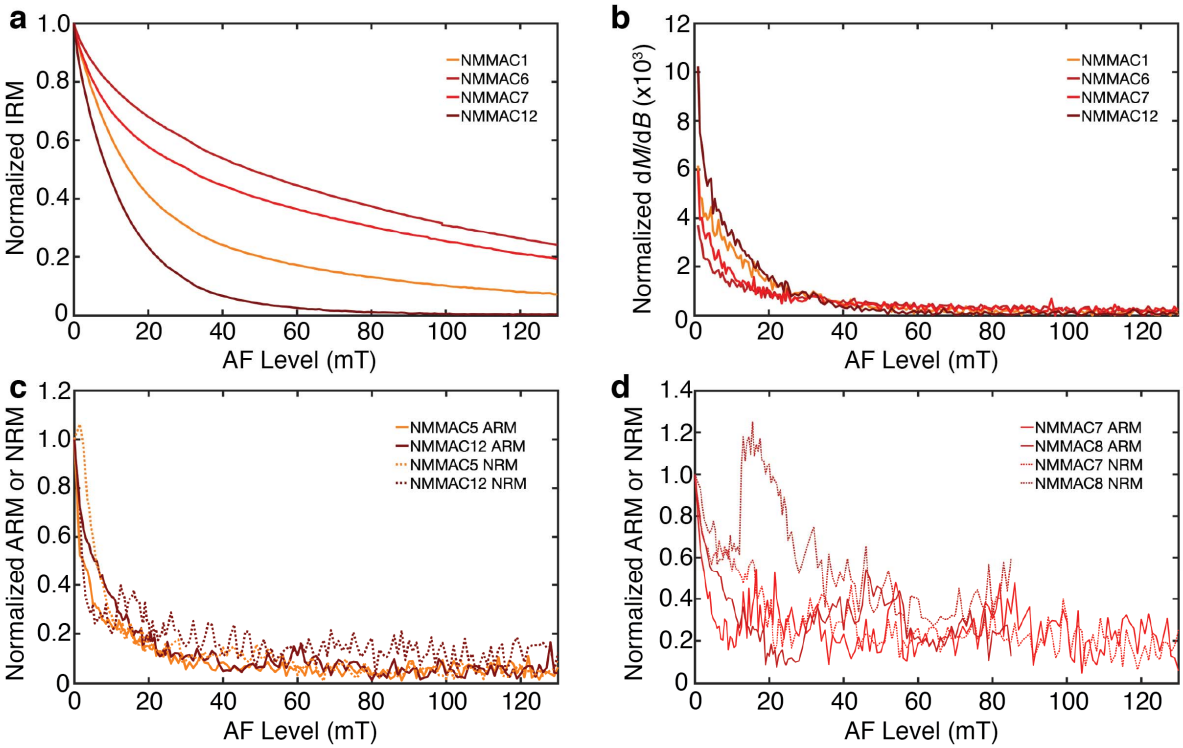

Figure 6: AF demagnetization of IRM and ARM in bulk samples using the SRM**. a)** Normalized IRM demagnetization as a function of AF level. **b)** IRM coercivity spectrum calculated by taking the derivative of the data in a) with respect to AF level. **c)** Normalized ARM demagnetization (solid line) and normalized NRM demagnetization (dashed line) versus AF level for two fusion-crusted samples. **d)** Normalized ARM demagnetization (solid line) and normalized NRM demagnetization (dashed line) versus AF level for two interior samples.

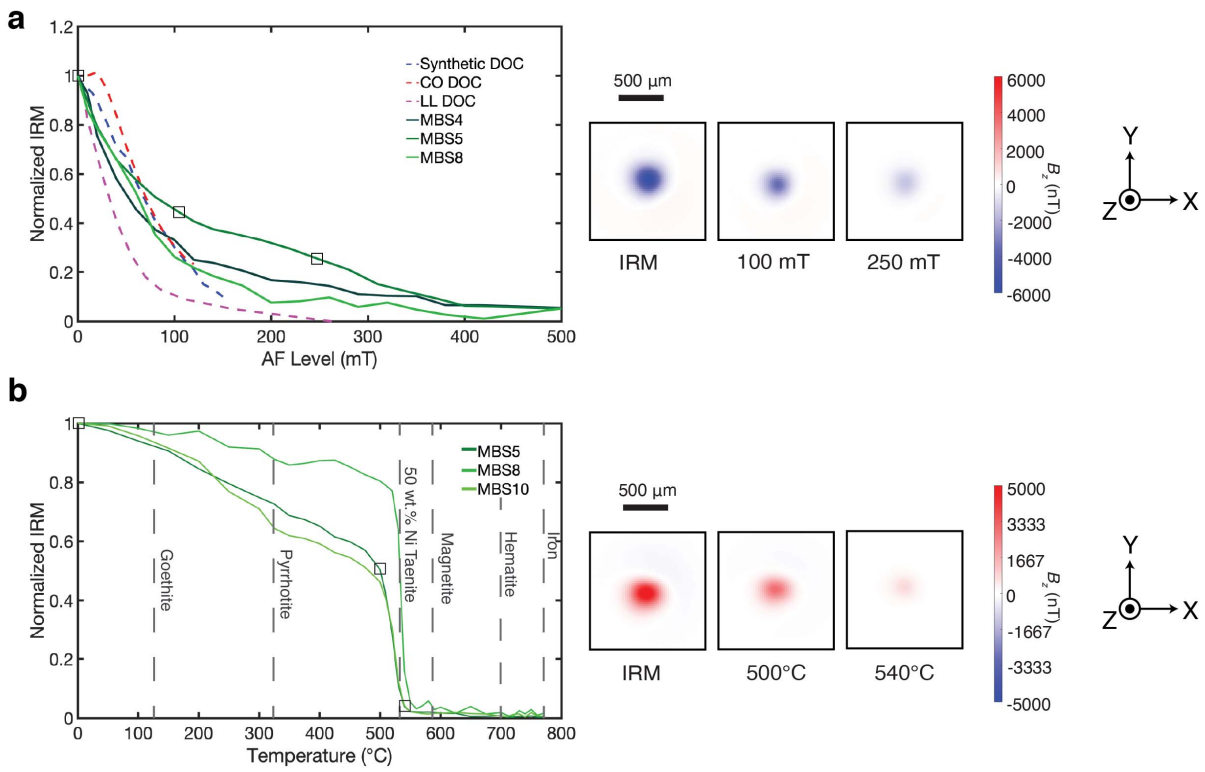

Figure 7. Demagnetization of IRM in MBSs using SQUID microscopy. **a)** AF demagnetization of a 1 T IRM for MBSs 4, 5, and 8 compared to a synthetic DOC (Lappe et al., 2011), type 3.00 CO (Dominion Range 08006) DOC (Borlina et al., 2021), and type 3.00 LL (Semarkona) DOC (Fu et al., 2014). Representative SQUID microscope maps showing the out-of-the-page component of the magnetic field at a height of 200 µm above the sample at selected field steps for MBS 5 are shown. The IRM was applied in the into-the-page (-*z*) direction. **b)** Thermal demagnetization of a 1 T IRM for MBSs 5, 8, and 12. The Curie temperatures of various ferromagnetic phases are shown by the dashed grey lines. Representative SQUID microscope maps at selected field steps for MBS 5 are shown. The IRM was applied in the out-of-the-page (+*z*) direction.

4 Discussion and Implications

4.1 Does Acapulco Have a Pre-Terrestrial Magnetic Record?

AF demagnetizations of NRMs in bulk samples and MBSs and their comparison to laboratory ARMs and IRMs indicate that Acapulco retains a pre-terrestrial magnetic record. We present three lines of evidence supporting this claim: 1) NRM/IRM < 1.5%, 2) directional scatter in MC components in bulk samples (i.e., passed Watson randomness test), and 3) lack of terrestrial weathering products.

The low NRM/IRM values (< 1.5%; Tables S1, S2) of the MBSs and bulk samples suggest that the interior of Acapulco was not substantially remagnetized by an external field

since falling to Earth. Since the expected proportion of magnetic recorders aligned with an Earth-strength external field during cooling (TRM efficiency) is ~1% of saturation IRM (McClelland, 1996; Yu et al., 2007), the NRM/IRM of the samples are consistent with a natural form of magnetization and not artificial contamination (e.g., from a hand magnet), which would produce NRM/IRM > 10% (Vervelidou et al., 2023).

The MCi/MCf components of bulk samples are scattered (Fig. 4) and the NRM directions of the MBSs vary in direction as well (Fig. 5). This is consistent with a lack of a strong overprint which would align the magnetizations of the bulk samples and MBSs. While curved fields around hand magnets can create NRMs with smoothly varying directions as function of depth in a sample and multiple exposures to hand magnets of different strengths from different orientations could create a scatter in the magnetization directions (Vervelidou et al., 2023), the low NRM/IRM values preclude this possibility for Acapulco. This is consistent with Acapulco being a fall given that magnet remagnetization mainly affects meteorite finds [e.g., (Weiss et al., 2008)].

Lastly, thermal demagnetization of IRM in MBSs shows that the remanence carriers are predominantly FeNi metal alloys (Fig. 7b). Common terrestrial phases that could form from weathering and oxidation of meteoritic metal include magnetite, hematite, and goethite (Uehara et al., 2012; Weiss et al., 2010). There is no observed drop in magnetization after heating to the Curie temperatures for those minerals.

While the LCf and LCi directions are statistically distinct and therefore Acapulco technically passes the fusion crust baked contact test, the directions' relative proximity could be interpreted as indicating uncertainty as to whether Acapulco actually passes that test. The proximity in the average directions could be due to a viscous remanent magnetization (VRM) acquired by the low-coercivity metal grains while sitting in Earth's magnetic field prior to NRM demagnetization. This interpretation is supported by the LCi/LCf paleointensities that are consistent with an Earth-strength field. Thus, the interior sample LCi directions would retain the VRM while the fusion-crusted LCf directions are an admixture of the VRM and a magnetization acquired during atmospheric entry. We note that the shapes of the fusion-crusted samples' ARM and NRM demagnetization curves are similar (Fig. 6c), suggesting that the LCf component in the samples are at least partially a TRM. This is expected since the fusion crust was a melt produced during atmospheric entry that cooled in Earth's magnetic field. In contract, the ARM and NRM demagnetization curves are different (Fig. 6d). Regardless of the fusion crust baked contact test results, the scatter in the MCi/MCf components indicates that the external field source of the LCi/LCf component did not fully magnetize Acapulco.

4.2 Can Acapulco Reliably Retain an Early Solar System Magnetization?

The two major ferromagnetic recorders in Acapulco are kamacite, identified by its composition, and tetrataenite. We interpret the high-Ni phases in MBSs and the plessitic microstructures to be tetrataenite on account of their high coercivities (up to 500 mT), changes in sample coercivity after heating, and Ni composition, in addition to further magnetic measurements discussed in the supplement. On the bulk scale, Acapulco's NRM, ARM, and

IRM are dominated by kamacite in the large interstitial metal grains. While there is evidence from our microscopy and magnetic data that tetrataenite is present in the plessitic cores of zoned taenite grains and MBSs, these precipitates' magnetizations are masked by the larger and more abundant kamacite. Kamacite that forms above its Curie temperature will record a TRM upon cooling. However, the morphology of the kamacite and the observed Ni gradients in the interstitial metal grains provide evidence of formation by subsolidus recrystallization of taenite as Ni is diffused out of the crystal structure. Hence, the kamacite in Acapulco would likely have recorded thermochemical remanent magnetization (TCRM), a form of remanence for which reliable paleointensity estimates have not yet been developed (Garrick-Bethell & Weiss, 2010). Furthermore, the various kamacite grains in the interstitial metal likely passed through their blocking temperatures at different times. Therefore, if a field was present in the region where ALs formed, the NRM of the bulk samples would be the sum of magnetizations acquired at different periods in time under potentially different field strengths and orientations. This could lead to scattered MCi/MCf directions. We note that the <5 GPa shock state of Acapulco ensures that its NRM is almost certainly not an SRM and that it has not been substantially demagnetizated or remagnetizated by shock pressures or heating since 4.55 Ga (Bezaeva et al., 2009; Weiss et al., 2010).

For MBSs, Acapulco's NRM, IRM, and ARM are carried by kamacite and tetrataenite. Tetrataenite would record a CRM during its formation by reordering of taenite when the meteorite cooled through 320°C (Einsle et al., 2018). Type I grains in MBSs are either present as pure kamacite or show evidence of subsolidus recrystallization in the form of a high-Ni rim. Thus, these grains either recorded a TRM during cooling or a similar TCRM as the kamacite in the interstitial metal grains in the bulk samples. Type II metal grains, which formed from decomposition of martensite into plessite at temperatures <500°C (Goldstein & Michael, 2006), have kamacite and tetrataenite that would record a TCRM. The TCRM for the kamacite would be recorded at the decomposition temperature and the TCRM for tetrataenite would be recorded at and below 320°C. We note that given the metallographic cooling rates reported for Acapulco [10^3 – 10^5 °C Ma^{-1} (Keil & McCoy, 2018)], the time difference between 780°C and 320°C could be 0.005 – 0.5 Ma. Therefore, similar to the bulk samples, the NRM of the MBSs is likely an aggregate of magnetizations produced at different times and possibly different external field conditions. As with the bulk samples, this could lead to scattered NRM and component directions.

Kamacite and tetrataenite that occupy the single domain (SD) or single vortex (SV) states can retain magnetizations stable against viscous relaxation over solar-system timescales (Mansbach et al., 2022; Shah et al., 2018). Electron holography of kamacite inclusions with a range of elongations in a synthetic DOC shows that grains up to ~250 nm occupy the SD or SV state (Lappe et al., 2013). In Acapulco bulk samples, the >50 μm size of the kamacite in the interstitial metal suggests that they are most likely multidomain and therefore poor magnetic recorders. However, sub-μm kamacite grains in MBSs could occupy the SV or SD state.

Non-interacting tetrataenite occupies the SD state between 6 nm and ~160 nm depending on its elongation (Mansbach et al., 2022). Unlike kamacite, tetrataenite does not have an SV state and transitions directly from the SD state to a two-domain state due to its high magnetocrystalline anisotropy (Mansbach et al., 2022). The sizes of the tetrataenite grains in the bulk samples (μm) and MBSs (μm to sub-μm) indicate that they are likely multidomain.

However, micromagnetic modeling of two-domain tetrataenite shows that the mineral can retain a stable magnetization against viscous relaxation and external remagnetization over the lifetime of the solar system (Mansbach et al., 2022). Therefore, the tetrataenite grains in Acapulco may hold a NRM dating back to near the time of its formation at 4.55 Ga.

4.3 How Can the Paleomagnetism and Rock Magnetic Properties of Acapulco Constrain the Parent Body's Interior Structure and Thermal Evolution?

The identification of tetrataenite and the lack of a cloudy zone provide a powerful cooling rate constraint on the AL parent body. In particular, the cloudy zone microstructure forms at an estimated maximum cooling rate of ~10,000°C Ma^{-1} (Maurel et al., 2019) while ordering from taenite to tetrataenite is reported to require an estimated maximum cooling rates below ~5,000°C Ma^{-1} (Yang & Goldstein, 2004). If these estimated critical cooling rates are accurate, this would mean that any meteorite with a high-Ni taenite rim containing tetrataenite should also have formed a cloudy zone in this region. However, we observe the presence of tetrataenite without a cloudy zone in Acapulco, indicating that either the reported critical cooling rates have overlapping uncertainties or Acapulco has very fine (20-30 nm) islands not visible in BSE images. Since we do not observe the >1 T coercivities characteristic of such fine islands (Mansbach et al., 2022), we suggest that the critical cooling rates have overlapping uncertainties and Acapulco cooled ~5,000°C Ma^{-1} at 320°C. This cooling rate is consistent with the reported metallographic cooling rates for acapulcoites (Keil & McCoy, 2018), albeit on the lower end of that range.

Our reported cooling rate at 320°C has important implications for the thermal evolution of the AL parent body. ALs must have been part of a body at least 2 km in radius based on recent cooling rates reported for lodranites (Lucas et al., 2022). For a 2 km radius body, ALs would have to be located within 10% of the radius of the center of the body. The depth of emplacement within the body decreases as the size of the body increases. Therefore, either the AL parent body was never disrupted prior to cooling through 320°C and instead underwent monotonic cooling through this temperature, or the body was disrupted above this temperature and ALs were later reaccreted into a secondary body of at least a few km in radius. The low cooling rate constraint imposed by tetrataenite suggests it is highly unlikely that the AL parent body was catastrophically disrupted and did not undergo at least partial recreation.

The presence of two ferromagnetic minerals in Acapulco that would have acquired their NRMs at different times enables the possibility of further constraining the thermal evolution of the parent body. Here, we present the methods by which a future paleomagnetic study of Acapulco or other members of the AL clan can elucidate the structure and history of the body. We consider that the parent body experienced one of four evolutionary paths (Fig. 8) after initial heating of the AL source region [outer 7-25 km (Neumann et al., 2018)] (ALSR), to peak temperatures of 1200°C [note that the deeper interior could have reached 1625°C as suggested by three-dimensional thermal modeling of the parent body (Neumann et al., 2018)]: 1) Continuous cooling without major disruption by impacts; 2) Catastrophic disruption at the time that the ALSR reached its peak temperature followed by re-accretion and final cooling; 3) Catastrophic disruption when the temperature of the ALSR ~500°C and then re-accretion and

final cooling; 4) Catastrophic disruption at the time that the ALSR reached its peak temperature followed by no reaccretion.

In each path, we start with the ALSR having reached its peak temperature and possessing an onion-shell structure as suggested by previous thermal models (Golabek et al., 2014; Neumann et al., 2018; Touboul et al., 2009). We allow for a chondritic crust to overlay a primitive achondritic layer that in turn overlies an igneous silicate region and possibly also a metallic core. In Case 1A, we consider a parent body evolution model in which the body possessed a tens of km radius metallic core that was capable of generating a dynamo (Bryson et al., 2019; Dodds et al., 2021; Weiss et al., 2010) on the tens-hundreds of Ma timescale like that found for IIE irons (Maurel et al., 2020; Maurel et al., 2021). In this scenario, the ALSR cools continuously from peak temperatures down to below 320°C. If the dynamo was present continuously, then both kamacite and tetrataenite in Acapulco would have acquired a NRM record of the dynamo during cooling through their blocking and ordering temperatures of 780°C (or lower as suggested by subsolidus recrystallization) and 320°C, respectively. However, the external field direction and strength may have changed between the times at which the NRMs were acquired by the two minerals or even changed while each mineral acquired its NRM.

In Case 1B, we consider the scenario in which the parent body continuously cooled, but there was either no core present or a core was present but was not able to generate a dynamo field. In this case, the parent body cools through the ordering and blocking temperatures of tetrataenite and kamacite but there is no external field recorded. In Case 2, the parent body was disrupted around ALSR peak temperatures and then reaccreted as solid fragments prior to ALSR cooling to 750°C [following (15)]. We expect that it is unlikely that a molten core formed that was sufficiently large to be able to generate a dynamo on the secondary body. Therefore, in both Cases 1b and 2, kamacite and tetrataenite would not have recorded a dynamo field.

In Case 3, the parent body was disrupted at a temperature after the ALSR cooled to below the blocking temperature of kamacite. In Case 3A, the parent body possessed a dynamo and the ALSR cooled through 780°C, which would enable the kamacite to retain a record of the external field. However, the body was then disrupted at ALSR temperatures ~500°C [as suggested by ref. (Göpel & Manhès, 2010)], and subsequently reaccreted. As before, it is highly unlikely that there would have been an advecting metal core capable of creating a dynamo field after reaccretion, and therefore the tetrataenite would not have recorded any field when the ALSR reached 320°C. Case 3B describes the evolution of a body that had no dynamo prior to disruption and therefore no dynamo field was recorded by the kamacite or tetrataenite.

In Case 4, the parent body is catastrophically disrupted into pieces <2 km in radius at ALSR peak temperatures and never reaccreted. As discussed previously, this path is not likely as ALs must have cooled at rates ~5,000°C Ma^{-1} at 320°C.

In summary, a thorough understanding of the paleomagnetic record of the tetrataenite and kamacite separately in ALs may distinguish between different parent body evolution paths. In the case where no field is recorded by either kamacite or tetrataenite, we would be unable to differentiate between Cases 1B, 2, or 3B. However, if both tetrataenite and kamacite show evidence for a dynamo field being present at their respective NRM acquisition temperatures, then the parent body was not likely disrupted and followed the path described in Case 1A. In this scenario, one potential explanation for the varying cooling rates reported for ALs could be impact unroofing of the material overlaying the ALs. Lastly, if kamacite contains an NRM record of a dynamo, but tetrataenite does not, then this would be consistent with catastrophic disruption below 780°C (i.e., Case 3A). However, an alternate explanation is that the dynamo ceased prior to reaching 320°C on a non-disrupted parent body.

Given the uniquely powerful ability of paleomagnetism to independently confirm the presence or absence of a dynamo on the AL parent body and therefore a metallic core larger than ~80 km in diameter (Weiss et al., 2010), further evaluation of the paleomagnetic record of ALs could provide valuable information to distinguish between the four abovementioned scenarios. However, as stated previously, the NRMs of both Acapulco bulk samples and MBSs are likely carried by at least two ferromagnetic minerals with different forms of TCRM acquired at different times. Therefore, it is necessary to more completely understand the acquisition of TCRMs by kamacite and tetrataenite prior to re-evaluating the paleomagnetic record of Acapulco. Regardless, the multidomain, interstitial metal grains in the bulk samples likely preclude a meaningful analyses of the NRM of bulk samples of Acapulco or of any AL containing metal grains of a similar size and abundance.

Future paleomagnetic studies should focus on MBSs as they contain magnetic recorders that are more likely to be SD or SV compared to the bulk samples. An additional option for AL paleomagnetic studies is to focus on those ALs with MBSs that cooled at rates >5,000 to 10,000°C Ma^{-1} and therefore would not possess tetrataenite. For example, the Monument Draw acapulcoite has a reported metallographic cooling rate of ~10^4 °C Ma^{-1} over the temperature range 600 – 350°C (McCoy et al., 1996). No lodranites have reported cooling rate around 320°C that are above 10^4 °C Ma^{-1} (Keil & McCoy, 2018). However, an alternative path is to identify very slowly cooled lodranites (<10^3 °C Ma^{-1}) and search for cloudy zones, which can be studied using X-ray photoemission electron microscopy (Bryson et al., 2014).

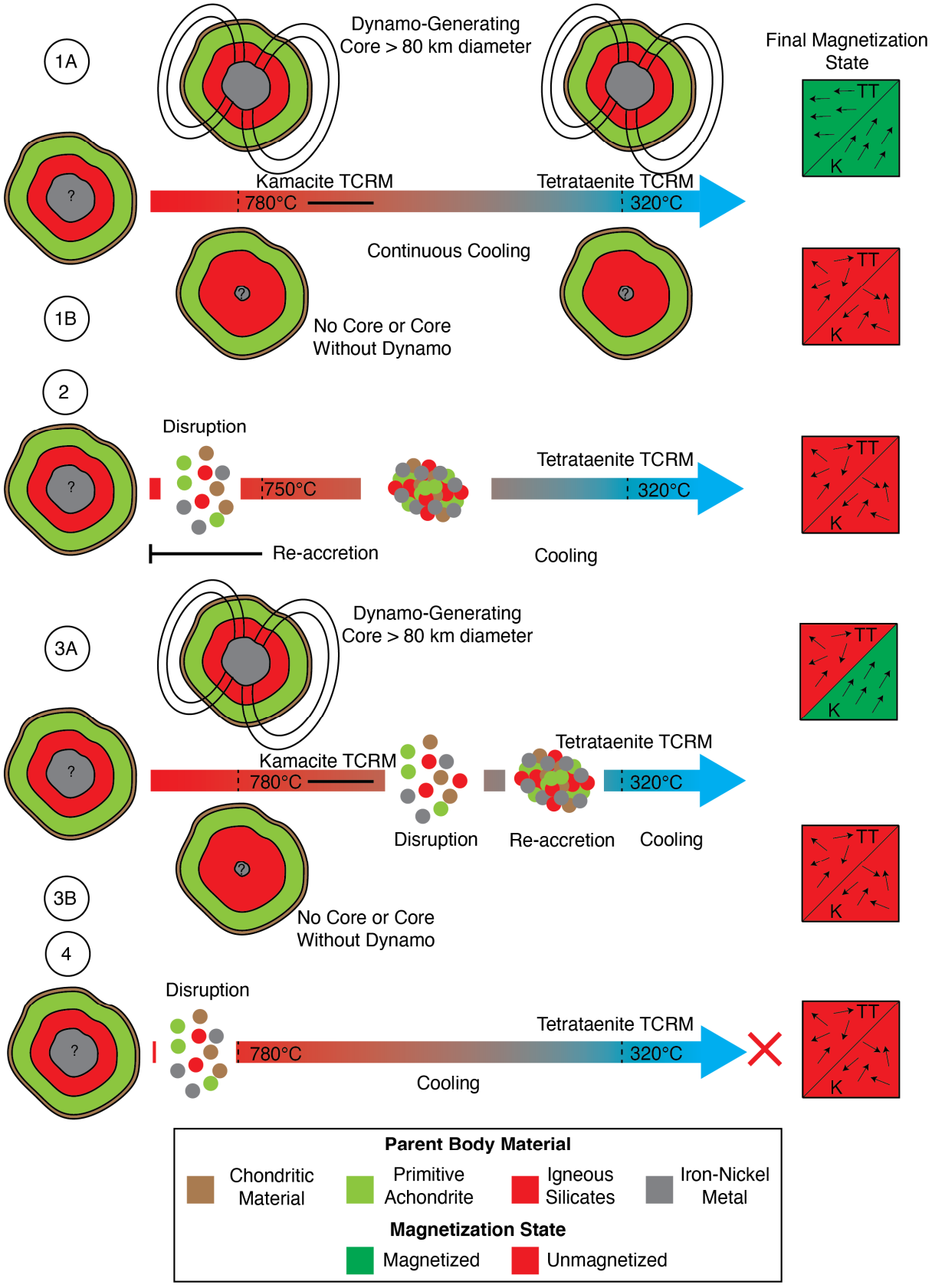
1A
Dynamo-Generating
Core > 80 km diameter
Final Magnetization
State
Kamacite TCRM
780°C
Tetrataenite TCRM
320°C
TT
K
Continuous Cooling
1B
No Core or Core
Without Dynamo
2
Disruption
750°C
Tetrataenite TCRM
320°C
Re-accretion
Cooling
3A
Dynamo-Generating
Core > 80 km diameter
Kamacite TCRM
780°C
Tetrataenite TCRM
320°C
Disruption
Re-accretion
Cooling
3B
No Core or Core
Without Dynamo
4
Disruption
Tetrataenite TCRM
780°C
320°C
Cooling
Parent Body Material
Chondritic Material
Primitive Achondrite
Igneous Silicates
Iron-Nickel Metal
Magnetization State
Magnetized
Unmagnetized

649 **Figure 8.** Parent body evolution scenarios. In Case 1, the parent body cooled without being
650 disrupted and possessed (Case 1A) or lacked (Case 1B) a dynamo. In Case 2, the parent body
651 was disrupted by impacts at peak temperatures and subsequently reaccreted to a form a
652 secondary body of at least 2 km in radius. No dynamo ever formed in this scenario. In Case 3,
653 the parent body began to cool but was later disrupted and reaccreted. If a dynamo was present
654 prior to disruption (Case 3A), then the kamacite would have acquired NRM in the field. In Case
655 4, the parent body was catastrophically disrupted at peak temperatures and never reaccreted. The
656 cooling rate threshold imposed by the presence of tetrataenite excludes Case 4 for the AL parent
657 body (as denoted by "×"). The final magnetization states of the kamacite and tetrataenite for each
658 Case are shown to the right. K = kamacite, T = tetrataenite.

5 Conclusions

- We present the results of a rock magnetic study of Acapulco and provide the initial results of the first paleomagnetic study of a primitive achondrite to determine if the parent body possessed a planetesimal dynamo.

- The major magnetic phases in bulk Acapulco samples are multidomain kamacite and tetrataenite, though there may be small enough tetrataenite grains in the plessite to be SD.

- The major magnetic phases in MBSs are kamacite and tetrataenite as well, but with smaller, potentially SD or SV grains sizes.

- Acapulco shows no evidence of remagnetization due to a collectors' magnets or terrestrial weathering and therefore can retain a pre-terrestrial magnetic record.

- Bulk samples are poor recorders due to large interstitial metal grains that dominate the measured NRM magnetization.

- The NRM magnetizations in MBSs are summations of multiple ferromagnetic minerals that would have acquired magnetizations at different times and in different forms, leading to complex NRMs that do not allow us to definitely conclude that a dynamo was present or absent on the parent body.

- No primary NRM components were isolated during AF demagnetization of MBS.

- The presence of tetrataenite indicates that Acapulco underwent slow cooling (~5,000°C Ma^{-1}) at 320°C. This suggests that it is highly unlikely that the parent body was catastrophically disrupted while Acapulco was at peak temperatures without subsequent reaccretion.

- Future paleomagnetic investigations of Acapulco that can interpet the magnetization of kamacite and tetrataenite separately may be able to determine the evolution of the parent body.

Acknowledgments

We acknowledge funding from NASA FINESST grant 80NSSC20K1366 and a private gift from Thomas F. Peterson, Jr. We thank Tim Grove for productive conversations about primitive achondrites and planetary differentiation and Caroline Ross for use of her vibrating sample magnetometer. We also thank Tim McCoy and the Smithsonian Institute staff for providing meteorite samples for this study.

Open Research

Magnetization files that contain data on the NRM demagnetization of all bulk samples and their magnetic properties used to draw the conclusions in this paper can be found on the Magnetics Information Consortium (MagIC) database via DOI:10.7288/V4/MAGIC/19872 (https://earthref.org/MagIC/19872/c29f1503-af3e-4983-a58e-4eef32d61523) as a zip file. The MagIC database DOI also contains .mat files with all SQUID maps taken of MBS magnetizations including NRM demagnetization, thermal demagnetization, ARM demagnetization, and IRM demagnetization.

References

Benedix, G. K., & Lauretta, D. S. (2006). *Thermodynamic constraints on the formation history of acapulcoites.* Lunar and Planetary Science Conference 37.

Bezaeva, N. S., Gattacceca, J., Rochette, P., & Sadykov, R. A. (2009). *Pressure demagnetization of ordinary chondrites up to 1.8 GPa: New experimental data*. American Geophysical Union Fall Meeting 2009.

Bild, R. W., & Wasson, J. T. (1976). The Lodran meteorite and its relationship to the ureilites. *Mineralogical Magazine, 40*(315), 721-735.

Borlina, C. S., Weiss, B. P., Bryson, J. F. J., Bai, X., Lima, E. A., Chatterjee, N., & Mansbach, E. N. (2021). Paleomagnetic evidence for a disk substructure in the early solar system. *Science Advances, 7*(42), eabj6928.

Bryson, J. F. J., Herrero-Albillos, J., Kronast, F., Ghidini, M., Redfern, S. A. T., van der Laan, G., & Harrison, R. J. (2014). Nanopaleomagnetism of meteoritic Fe–Ni studied using X-ray photoemission electron microscopy. *Earth and Planetary Science Letters, 396*, 125-133.

Bryson, J. F. J., Neufeld, J. A., & Nimmo, F. (2019). Constraints on asteroid magnetic field evolution and the radii of meteorite parent bodies from thermal modelling. *Earth and Planetary Science Letters, 521*, 68-78.

Bryson, J. F. J., Weiss, B. P., Harrison, R. J., Herrero-Albillos, J., & Kronast, F. (2017). Paleomagnetic evidence for dynamo activity driven by inward crystallisation of a metallic asteroid. *Earth and Planetary Science Letters, 472*, 152-163.

Dhaliwal, J. K., Day, J. M. D., Corder, C. A., Tait, K. T., Marti, K., Assayag, N., et al. (2017). Early metal-silicate differentiation during planetesimal formation revealed by acapulcoite and lodranite meteorites. *Geochimica et Cosmochimica Acta, 216*, 115-140.

Dodds, K. H., Bryson, J. F. J., Neufeld, J. A., & Harrison, R. J. (2021). The thermal evolution of planetesimals during accretion and differentiation: Consequences for dynamo generation by thermally-driven convection. *Journal of Geophysical Research: Planets, 126*(3).

Dos Santos, E., Gattacceca, J., Rochette, P., Fillion, G., & Scorzelli, R. B. (2015). Kinetics of tetrataenite disordering. *Journal of Magnetism and Magnetic Materials, 375*, 234-241.

Dunlop, D. J., & Argyle, K. S. (1997). Thermoremanence, anhysteretic remanence and susceptibility of submicron magnetites: Nonlinear field dependence and variation with grain size. *Journal of Geophysical Research: Solid Earth, 102*(B9), 20199-20210.

Einsle, J. F., Eggeman, A. S., Martineau, B. H., Saghi, Z., Collins, S. M., Blukis, R., et al. (2018). Nanomagnetic properties of the meteorite cloudy zone. *Proceedings of the National Academy of Sciences, 115*(49), E11436-E11445.

El Goresy, A., Zinner, E., Pellas, P., & Caillet, C. (2005). A menagerie of graphite morphologies in the Acapulco meteorite with diverse carbon and nitrogen isotopic signatures: Implications for the evolution history of acapulcoite meteorites. *Geochimica et Cosmochimica Acta, 69*(18), 4535-4556.

Fu, R. R., Lima, E. A., Volk, M. W. R., & Trubko, R. (2020). High-sensitivity moment magnetometry with the quantum diamond microscope. *Geochemistry, Geophysics, Geosystems, 21*(8), e2020GC009147.

Fu, R. R., Weiss, B. P., Lima, E. A., Harrison, R. J., Bai, X.-N., Desch, S. J., et al. (2014). Solar nebula magnetic fields recorded in the Semarkona meteorite. *Science, 346*(6213), 1089-1092.

Garrick-Bethell, I., & Weiss, B. P. (2010). Kamacite blocking temperatures and applications to lunar magnetism. *Earth and Planetary Science Letters, 294*(1), 1-7.

Garrick-Bethell, I., Weiss, B. P., Shuster, D. L., & Buz, J. (2009). Early lunar magnetism. *Science, 323*(5912), 356-359.

Glenn, D. R., Fu, R. R., Kehayias, P., Sage, D. L., Lima, E. A., Weiss, B. P., & Walsworth, R. L. (2017). Micrometer-scale magnetic imaging of geological samples using a quantum diamond microscope. *Geochemistry, Geophysics, Geosystems, 18*(8), 3254-3267.

Golabek, G. J., Bourdon, B., & Gerya, T. V. (2014). Numerical models of the thermomechanical evolution of planetesimals: Application to the acapulcoite-lodranite parent body. *Meteoritics & Planetary Science, 49*(6), 1083-1099.

Goldstein, J. I., & Michael, J. R. (2006). The formation of plessite in meteoritic metal. *Meteoritics & Planetary Science, 41*(4), 553-570.

Göpel, C., & Manhès, G. (2010). The thermal history of the Acapulco meteorite and its parent body deduced from U/Pb systematics in mineral separates and bulk rock fragments. *Comptes Rendus Geoscience, 342*(1), 53-59.

Greenwood, R. C., Burbine, T. H., Miller, M. F., & Franchi, I. A. (2017). Melting and differentiation of early-formed asteroids: The perspective from high precision oxygen isotope studies. *Geochemistry, 77*(1), 1-43.

Greenwood, R. C., Franchi, I. A., Gibson, J. M., & Benedix, G. K. (2012). Oxygen isotope variation in primitive achondrites: The influence of primordial, asteroidal and terrestrial processes. *Geochimica et Cosmochimica Acta, 94*, 146-163.

Keil, K., & McCoy, T. J. (2018). Acapulcoite-lodranite meteorites: Ultramafic asteroidal partial melt residues. *Geochemistry, 78*(2), 153-203.

Khokhlov, A., & Hulot, G. (2015). Principal component analysis of palaeomagnetic directions: Converting a maximum angular deviation (MAD) into an α_{95} angle. *Geophysical Journal International, 204*(1), 274-291.

Kirschvink, J. L. (1980). The least-squares line and plane and the analysis of palaeomagnetic data. *Geophysical Journal International, 62*(3), 699-718.

Lappe, S. L. L., Church, N. S., Kasama, T., da Silva Fanta, A. B., Bromiley, G., Dunin-Borkowski, R. E., et al. (2011). Mineral magnetism of dusty olivine: A credible recorder of pre-accretionary remanence. *Geochemistry, Geophysics, Geosystems, 12*(12), Q12Z35.

Lappe, S. L. L., Feinberg, J. M., Muxworthy, A. R., & Harrison, R. J. (2013). Comparison and calibration of nonheating paleointensity methods: A case study using dusty olivine. *Geochemistry, Geophysics, Geosystems, 14*(7), 2143-2158.

Lima, E. A., & Weiss, B. P. (2016). Ultra-high sensitivity moment magnetometry of geological samples using magnetic microscopy: Ultra-sensitive moment magnetometry. *Geochemistry, Geophysics, Geosystems, 17*(9), 3754-3774.

Lucas, M. P., Dygert, N., Ren, J., Hesse, M. A., Miller, N. R., & McSween, H. Y. (2022). Thermochemical evolution of the acapulcoite–lodranite parent body: Evidence for fragmentation-disrupted partial differentiation. *Meteoritics & Planetary Science*, 2248-2275.

Mansbach, E. N., Shah, J., Williams, W., Maurel, C., Bryson, J. F. J., & Weiss, B. P. (2022). Size ranges of magnetic domain states in tetrataenite. *Geochemistry, Geophysics, Geosystems, 23*(11).

Maurel, C., Bryson, J. F. J., Lyons, R. J., Ball, M. R., Chopdekar, R. V., Scholl, A., et al. (2020). Meteorite evidence for partial differentiation and protracted accretion of planetesimals. *Science Advances, 6*(30), eaba1303.

Maurel, C., Bryson, J. F. J., Shah, J., Chopdekar, R. V., T. Elkins-Tanton, L., A. Raymond, C., & Weiss, B. P. (2021). A long-lived planetesimal dynamo powered by core crystallization. *Geophysical Research Letters, 48*(6), e2020GL091917.

Maurel, C., Weiss, B. P., & Bryson, J. F. J. (2019). Meteorite cloudy zone formation as a quantitative indicator of paleomagnetic field intensities and cooling rates on planetesimals. *Earth and Planetary Science Letters, 513*, 166-175.

McClelland, E. (1996). Theory of CRM acquired by grain growth, and its implications for trm discrimination and palaeointensity determination in igneous rocks. *Geophysical Journal International, 126*(1), 271-280.

McCoy, T. J., Keil, K., Clayton, R. N., Mayeda, T. K., Bogard, D. D., Garrison, D. H., et al. (1996). A petrologic, chemical, and isotopic study of Monument Draw and comparison with other acapulcoites: Evidence for formation by incipient partial melting. *Geochimica et Cosmochimica Acta, 60*(14), 2681-2708.

McCoy, T. J., Keil, K., Muenow, D. W., & Wilson, L. (1997). Partial melting and melt migration in the acapulcoite-lodranite parent body. *Geochimica et Cosmochimica Acta, 61*(3), 639-650.

Neumann, W., Henke, S., Breuer, D., Gail, H., Schwarz, W. H., Trieloff, M., et al. (2018). Modeling the evolution of the parent body of acapulcoites and lodranites: A case study for partially differentiated asteroids. *Icarus, 311*, 146-169.

Nichols, C. I. O., Krakow, R., Herrero-Albillos, J., Kronast, F., Northwood-Smith, G., & Harrison, R. J. (2018). Microstructural and paleomagnetic insight into the cooling history of the IAB parent body. *Geochimica et Cosmochimica Acta, 229*, 1-19.

Palme, H., Schultz, L., Spettel, B., Weber, H. W., Wänke, H., Michel-Levy, M. C., & Lorin, J. C. (1981). The Acapulco meteorite: Chemistry, mineralogy and irradiation effects. *Geochimica et Cosmochimica Acta, 45*(5), 727-752.

Renne, P. R. (2000). $^{40}Ar/^{39}Ar$ age of plagioclase from acapulco meteorite and the problem of systematic errors in cosmochronology. *Earth and Planetary Science Letters, 175*(1-2), 13-26.

Rochette, P., Gattacceca, J., Bourot-Denise, M., Consolmagno, G., Folco, L., Kohout, T., et al. (2009). Magnetic classification of stony meteorites: 3. Achondrites. *Meteoritics & Planetary Science, 44*(3), 405-427.

824 Shah, J., Williams, W., Almeida, T. P., Nagy, L., Muxworthy, A. R., Kovács, A., et al. (2018).
825 The oldest magnetic record in our solar system identified using nanometric imaging and
826 numerical modeling. *Nature Communications, 9*(1).
827 Stephenson, A. (1993). Three-axis static alternating field demagnetization of rocks and the
828 identification of natural remanent magnetization, gyroremanent magnetization, and
829 anisotropy. *Journal of Geophysical Research: Solid Earth, 98*(B1), 373-381.
830 Suavet, C., Weiss, B. P., & Grove, T. L. (2014). Controlled-atmosphere thermal demagnetization
831 and paleointensity analyses of extraterrestrial rocks. *Geochemistry Geophysics*
832 *Geosystems, 15*(7), 2733-2743.
833 Swartzendruber, L. J., Itkin, V. P., & Alcock, C. B. (1991). The Fe-Ni (iron-nickel) system.
834 *Journal of Phase Equilibria, 12*(3), 288-312.
835 Tauxe, L. (2010). *Essentials of paleomagnetism*. University of California Press. 512.
836 Tauxe, L., & Staudigel, H. (2004). Strength of the geomagnetic field in the cretaceous normal
837 superchron: New data from submarine basaltic glass of the Troodos Ophiolite.
838 *Geochemistry, Geophysics, Geosystems, 5*(2), Q02H06.
839 Tikoo, S. M., Weiss, B. P., Buz, J., Lima, E. A., Shea, E. K., Melo, G., & Grove, T. L. (2012).
840 Magnetic fidelity of lunar samples and implications for an ancient core dynamo. *Earth*
841 *and Planetary Science Letters, 337-338*, 93-103.
842 Tikoo, S. M., Weiss, B. P., Cassata, W. S., Shuster, D. L., Gattacceca, J., Lima, E. A., et al.
843 (2014). Decline of the lunar core dynamo. *Earth and Planetary Science Letters, 404*, 89-
844 97.
845 Touboul, M., Kleine, T., Bourdon, B., Van Orman, J. A., Maden, C., & Zipfel, J. (2009). Hf–W
846 thermochronometry: II. Accretion and thermal history of the acapulcoite–lodranite parent
847 body. *Earth and Planetary Science Letters, 284*(1-2), 168-178.
848 Uehara, M., Gattacceca, J., Rochette, P., Demory, F., & Valenzuela, E. M. (2012). Magnetic
849 study of meteorites recovered in the Atacama Desert (Chile): Implications for meteorite
850 paleomagnetism and the stability of hot desert surfaces. *Physics of the Earth and*
851 *Planetary Interiors, 200-201*, 113-123.
852 Vervelidou, F., Weiss, B. P., & Lagroix, F. (2023). Hand magnets and the destruction of ancient
853 meteorite magnetism. *Journal of Geophysical Research: Planets, 128*(4).
854 Wang, H., Weiss, B. P., Bai, X. N., Downey, B. G., Wang, J., Wang, J., et al. (2017). Lifetime of
855 the solar nebula constrained by meteorite paleomagnetism. *Science, 355*(6325), 623-627.
856 Weisberg, M. W., McCoy, T. J., & Krot, A. N. (2006). Systematics and evaluation of meteorite
857 clasification. In *Meteorites and the early solar system ii*.
858 Weiss, B. P., Berdahl, J. S., Elkins-Tanton, L., Stanley, S., Lima, E. A., & Carporzen, L. (2008).
859 Magnetism on the angrite parent body and the early differentiation of planetesimals.
860 *Science, 322*(5902), 713-716.
861 Weiss, B. P., & Elkins-Tanton, L. T. (2013). Differentiated planetesimals and the parent bodies
862 of chondrites. *Annual Review of Earth and Planetary Sciences, 41*(1), 529-560.
863 Weiss, B. P., Gattacceca, J., Stanley, S., Rochette, P., & Christensen, U. R. (2010).
864 Paleomagnetic records of meteorites and early planetesimal differentiation. *Space Science*
865 *Reviews, 152*(1-4), 341-390.
866 Weiss, B. P., Lima, E. A., Fong, L. E., & Baudenbacher, F. J. (2007). Paleomagnetic analysis
867 using squid microscopy. *Journal of Geophysical Research, 112*(B9).

Yang, J., & Goldstein, J. I. (2004). Magnetic contribution to the interdiffusion coefficients in bcc (α) and fcc (γ) Fe-Ni alloys. *Metallurgical and Materials Transactions A, 35*(6), 1681-1690.

Yang, J., & Goldstein, J. I. (2005). The formation of the Widmanstätten structure in meteorites. *Meteoritics & Planetary Science, 40*(2), 239-253.

Yang, J., Goldstein, J. I., & Scott, E. R. D. (2007). Iron meteorite evidence for early formation and catastrophic disruption of protoplanets. *Nature, 446*(7138), 888-891.

Yu, Y., Tauxe, L., & Gee, J. S. (2007). A linear field dependence of thermoremanence in low magnetic fields. *Physics of the Earth and Planetary Interiors, 162*(3), 244-248.

Zipfel, J., Palme, H., Kennedy, A. K., & Hutcheon, I. D. (1995). Chemical composition and origin of the Acapulco meteorite. *Geochimica et Cosmochimica Acta, 59*(17), 3607-3627.